Full-Wave Removal of Internal Antenna Effects and Antenna–Medium Interactions for Improved Ground-Penetrating Radar Imaging

Albéric De Coster and Sébastien Lambot, *Member, IEEE*

***Abstract*— Antenna effects alter the detection of buried objects during ground-penetrating radar (GPR) surveys. In this paper, we propose a novel approach based on full-wave inversion to filter out antenna effects from GPR data. The approach, which is exact for locally planar layered media, resorts to a recently developed electromagnetic model that takes advantage of an intrinsic, closed-form solution of Maxwell's equations to describe the antenna–medium system. As any multilayered medium can be reduced to a half-space medium with effective, frequency-dependent, global reflection coefficients, the method consists in inverting the radar data to retrieve a frequency-dependent, half-space complex conductivity. Converted into the time domain, this quantity represents the filtered radar image. We validated the approach through numerical simulations and laboratory experiments with pipes buried in a sandbox. The results demonstrated the validity of the concept and showed that the filtered radar images include only medium reflections, which means an easier interpretation in terms of medium structures. Antenna radiation pattern effects are, however, not removed. This physically based approach including the full-wave antenna model appears to be very promising for improved subsurface imaging and provides the basis for multifrequency GPR data fusion as the source is inherently normalized.**

***Index Terms*— Antenna effects removal, full-wave inversion (FWI), Green's functions, ground-penetrating radar (GPR), inverse modeling.**

I. Introduction

GROUND-PENETRATING radar (GPR) is a nondestructive tool which has raised a substantial interest in many applications, especially in subsurface characterization. It provides qualitative and quantitative information through the analysis of the electromagnetic waves backscattered at electromagnetic contrasts. Analyzing GPR images allows detecting and locating buried objects (pipes, mines, etc.) under favorable environmental conditions [1], [2]. However, the detection capability is affected by the clutter, i.e., the signals not being backscattered by the targets but having similar spectral characteristics and occurring in the same acquisition time window [3]. The clutter generally tends to dominate the data and to obscure the information related to the targets of interest. The development of appropriate techniques for clutter reduction is therefore essential to improve the GPR image analysis. Clutter reduction constitutes a challenging task as undesired reflections arise from various different factors: antenna effects including antenna–medium interactions, soil roughness, spatial distribution of soil electromagnetic properties, and diffuse scattering reflectors [4]–[7].

Numerous clutter reduction approaches have been developed in order to facilitate the GPR data interpretation. They have provided various performances regarding the enhancement of GPR images. The early time gating approach, i.e., setting to zero the time window containing the early part of the radar waveforms, is one of the most commonly used techniques [8]. However, the selection of an appropriate time window represents a challenging task when the antenna is close from the ground surface and/or when objects are shallowly buried, as it causes constructive and destructive interferences due to the overlapping reflections (antenna–medium coupling). Background subtraction (BS) strategies such as moving average or moving median subtraction are widely used to remove a part of the antenna effects [9]–[12]. These approaches generally assume that the properties and roughness of the medium surrounding the target are slowly varying with the spatial position. Strategies such as amplitude shifted and scaled BS are more efficient when roughness is significant [13]. Yet, these methods cannot completely eliminate the clutter. Moreover, they alter the field backscattered by the target (e.g., constant reflections are removed).

Parametric and statistically based methods have also been proposed to remove undesired reflections originating from the surface or other sources [14]–[16]. Some of these methods are sensitive to the spatial variations of the soil permittivity or surface roughness. van der Merwe and Gupta [16] proposed a parametric clutter removal approach based on an iterative signal processing algorithm to estimate unknown parameters in basis functions and reduce the clutter. The method presents the advantage of taking into account the presence of shallowly buried objects but requires the reference signatures of these ones. Different other studies used principal

Manuscript received January 12, 2018; revised May 2, 2018; accepted June 18, 2018. Date of publication July 26, 2018; date of current version December 24, 2018. This work was supported in part by the Walloon Region through the "SENSPORT" Project undertaken in the framework of the WBGreen Research Program under Grant 1217720, in part by the SEWERMAPPER Project (EraSME) under Grant 1410258, in part by the Fonds National de la Recherche Scientifique, Belgium, in part by EU through COST Action TU1208 "Civil Engineering Applications of Ground Penetrating Radar," and in part by the FSO Project under Grant 1610078. *(Corresponding author: Albéric De Coster.)*

The authors are with the Earth and Life Institute, Université catholique de Louvain, 1348 Louvain-la-Neuve, Belgium (e-mail: alberic.decoster@uclouvain.be).

Color versions of one or more of the figures in this paper are available online at http://ieeexplore.ieee.org.

Digital Object Identifier 10.1109/TGRS.2018.2852486

component analysis and independent component analysis multivariable techniques to separate and filter out the clutter from the backscattered signals [17]–[21]. These statistically based strategies provide satisfying results but the discrimination between the components coming from the object and the clutter is often achieved by visual inspection [22]. Moreover, the performance of this group of methods depends on the clutter model and the validity of the hypotheses assumed to estimate the parameters and statistical features.

In addition to the approaches previously described, we can identify other strategies that have been developed and used to remove clutter. Among others, we can cite the 2-D digital filter [22], the Kalman filter [23]–[26], and the differential configuration approach [27]–[29]. The differential configuration approach exploits the difference between the total fields acquired with two identical antennas. These antennas are located at the same height above the air–soil interface and are positioned symmetrically on both sides of the transmitting antenna [28]. The subtraction of the two signals allows erasing the direct coupling between the transmitter and the receiver and permits to get rid of the incident field from the data in the frequency domain. Very recently, a novel differential GPR configuration was developed considering two receiving antennas positioned at different heights above the investigated medium [29]. In contrast to the previous methodology, it preserves information on the layered structure of the medium but does not remove directly the air–soil interface.

A different way of removing the clutter in the GPR data can be done by resorting to a parametric statistical physically based solution. In that respect, Lambot *et al.* [30] proposed a physically based filtering procedure aiming at removing the soil surface reflection and antenna effects from the far-field GPR data. The underlying method, which relies on an integrated antenna–medium model, was first applied on the multilayered media [30] and then combined with a time-domain phase-shift migration to be used in the presence of objects [5]. The studies demonstrated the benefits of the proposed approach compared with the traditional BS methods. However, due to hypotheses assumed in the electromagnetic model, the methodology was only valid under far-field conditions, namely, the distance between the antenna and the medium should be larger than 1.2 times the antenna aperture size [31]. Indeed, under near-field conditions, the assumption of a homogeneous field over the antenna aperture as adopted in [30] does not hold anymore, because the medium properties and the medium–antenna distance influence the backscattered field distribution over the antenna aperture.

More recently, Lambot and André [32] and Lambot [33] generalized this intrinsic antenna model to near-field conditions and, therefore, tackled this issue. In particular, the model accounts for near-field antenna–medium coupling and multiple antenna internal reflections through intrinsic global transmission and reflection coefficient functions. Wave propagation in the 3-D layered media is modeled using 3-D Green's functions. However, in contrast to the far-field configuration, the near-field configuration does not allow the radar equation to be analytically inverted and, hence, to filter out antenna effects. An the antenna is close to the medium (improved penetration depth) would, however, be beneficial to optimize the interpretation of the information provided by the sensor.

In this paper, we propose a new physically based full-wave antenna effects filtering method valid under near-field conditions. This paper brings the development made in [32] one step further as, to the best of the authors' knowledge, such a filtering method has not been proposed before. The methodology resorts to a specific inverse modeling strategy and exploits the full-wave inversion (FWI) of the radar data to estimate a half-space, frequency-dependent complex conductivity. When converted into the time domain, this quantity shows all reflections within the equivalent multilayered medium, without any antenna internal and antenna–medium reflections. We tested the proposed approach using numerical experiments and compared the results with the analytical solution which is valid under far-field conditions. We also applied the near-field method under laboratory conditions for radar measurements performed over pipes buried in a sandbox and compared results with the filtered image provided by the average background removal approach and an ideal filtered image.

II. Near-Field Antenna Model

A. Model Formulation

The model relies on a full-wave solution of 3-D Maxwell's equations accounting for antenna wave propagation in the planar layered media. The antenna is modeled by considering a source made up of a set of infinitesimal electric dipoles and a receiver consisting of an equivalent set of points where the backscattered field is calculated. The distribution of the backscattered field over the antenna aperture is thereby decomposed into a series of homogeneous fields by resorting to the superposition principle. The number of points to choose is finite and depends on the complexity of the backscattered field distribution. It actually depends on: 1) the geometry of the antenna and 2) the distance between the multilayered medium and the antenna aperture (see also [31]). Presently, the optimal number of points is chosen on a case-by-case basis following a trial and error approach. As shown in the previous study [34], a too small number of points would generate accuracy problems, whereas a too large number of points would increase the computation time associated with inversions. Future research will focus on a better understanding of the required number of points in order to provide an automated way to determine it. The wave propagation between the radar reference plane and these source/field points is described through complex and frequency-dependent global reflection and transmission coefficients. These coefficients account for the variations of impedance within the antenna. Taking these complex phenomena into account constitutes the benefit of this model compared with other existing approaches. The model, in particular, permits to inherently describe antenna–medium coupling. The generalized radar equation is formulated in the frequency domain as follows [32]:

$$S(\omega) = \frac{b(\omega)}{a(\omega)} = T_0(\omega) + \mathbf{T_s}(\mathbf{I_M} - \mathbf{G^0 R_s})^{-1}\mathbf{G T_i} \qquad (1)$$

with

$$\mathbf{T_i} = \begin{bmatrix} T_{i,1}(\omega) & T_{i,2}(\omega) & \cdots & T_{i,M}(\omega) \end{bmatrix}^T \tag{2}$$

$$\mathbf{T_s} = \begin{bmatrix} T_{s,1}(\omega) & T_{s,2}(\omega) & \cdots & T_{s,M}(\omega) \end{bmatrix} \tag{3}$$

$$\mathbf{R_s} = \mathrm{diag}\left(\begin{bmatrix} R_{s,1}(\omega) & R_{s,2}(\omega) & \cdots & R_{s,M}(\omega) \end{bmatrix}\right) \tag{4}$$

$$\mathbf{G} = \begin{bmatrix} G_{11}(\omega) & G_{12}(\omega) & \cdots & G_{1M}(\omega) \\ G_{21}(\omega) & G_{22}(\omega) & \cdots & G_{2M}(\omega) \\ \vdots & \vdots & & \vdots \\ G_{M1}(\omega) & G_{M2}(\omega) & \cdots & G_{MM}(\omega) \end{bmatrix} \tag{5}$$

and

$$\mathbf{G^0} = \begin{bmatrix} G^0_{11}(\omega) & G^0_{12}(\omega) & \cdots & G^0_{1M}(\omega) \\ G^0_{21}(\omega) & G^0_{22}(\omega) & \cdots & G^0_{2M}(\omega) \\ \vdots & \vdots & & \vdots \\ G^0_{M1}(\omega) & G^0_{M2}(\omega) & \cdots & G^0_{MM}(\omega) \end{bmatrix} \tag{6}$$

where $S(\omega)$ denotes the radar signal, i.e., the ratio between the backscattered field $b(\omega)$ and the incident field $a(\omega)$ at the radar reference plane, ω refers to the angular frequency, I_M is the M-order identity matrix, where M is the number of point sources or field points, $T_0(\omega)$ is the global transmission/global reflection coefficient of the antenna in free space, $T_{i,.}(\omega)$ denotes the global transmission coefficient for the fields incident from the radar reference plane onto the source points, $T_{s,.}(\omega)$ is the global transmission coefficient for the fields incident from the source points onto the radar reference plane, and $R_{s,.}(\omega)$ is the global reflection coefficient for fields incident from the layered medium onto the field points and, in particular, accounts for infinite wave reflections between the antenna and the medium (antenna–medium coupling). Finally, $G_{..}(\omega)$ and $G^0_{..}(\omega)$ denote the layered medium Green's functions, i.e., the exact solutions of the 3-D Maxwell's equations for describing wave propagation in the planar multilayered media. $G_{..}(\omega)$ and $G^0_{..}(\omega)$ refer, respectively, to the transmitter–receiver and receiver–receiver Green's functions. The antenna characteristic coefficients are determined using a specific calibration procedure. We refer to Lambot and André [32] for the detailed description of the calibration methodology.

If far-field conditions are respected [31], we can assume that the backscattered field over the antenna aperture is homogeneous, and hence, the number of source/field points M is equal to 1. In monostatic mode, (1) that expresses the relation between the measured field and the 3-D layered medium Green's function reduces to [30]

$$S(\omega) = \frac{b(\omega)}{a(\omega)} = R_i(\omega) + \frac{G_{11}(\omega)T_1(\omega)}{1 - G_{11}(\omega)R_{s,1}(\omega)} \tag{7}$$

with $R_i(\omega)$ corresponding to $T_0(\omega)$ for the zero-offset source–receiver point and T_1 corresponding to the product $T_{s,1}T_{i,1}$.

B. Green's Function

The Green's function $G_{..}(\omega)$ is defined as the x-component of the backscattered electric field at the field point for a unit strength x-directed electric source situated at the same location. The spatial domain Green's function is defined as

$$G_{..} = \frac{1}{8\pi}\int_0^{+\infty} \widetilde{G}_{..}(k_\rho)k_\rho dk_\rho \tag{8}$$

where $\widetilde{G}_{..}(k_\rho)$ is the spectral Green's function that is computed as follows:

$$\widetilde{G}_{..}(k_\rho) = \left[J_0(k_\rho\rho)\left(\frac{\Gamma_0 R_0^{\mathrm{TM}}}{\eta_0} - \frac{\zeta_0 R_0^{\mathrm{TE}}}{\Gamma_0}\right) - J_2(k_\rho\rho) \cos(2\theta)\left(\frac{\Gamma_0 R_0^{\mathrm{TM}}}{\eta_0} + \frac{\zeta_0 R_0^{\mathrm{TE}}}{\Gamma_0}\right)\right]\exp(-2\Gamma_0 h_0) \tag{9}$$

where J_0 and J_2 are, respectively, the first kind zero- and second-order Bessel's functions, ρ and θ are, respectively, the distance and angle in the xy plane between the field and source points, subscript 0 refers to the free space upper half-space, h_0 is the distance between the source and field points and the first interface of the layered medium, Γ_0 is the vertical wavenumber defined as $\Gamma_0 = (k_\rho^2 + \zeta_0\eta_0)^{1/2}$, with $\zeta_0 = j\omega\mu_0$, $\eta_0 = \sigma_0 + j\omega\epsilon_0$, and μ_0, ε_0, and σ_0 represent the magnetic permeability, dielectric permittivity, and electrical conductivity of the upper half-space layer, respectively. R_0^{TM} and R_0^{TE} are, respectively, the transverse magnetic (TM) and the transverse electric (TE) global reflection coefficients accounting for all reflections in the multilayered medium [35]. The global TM-mode and TE-mode reflection coefficients at interface n $(n = 0, \ldots, N-1)$ are defined as follows:

$$R_n^{\mathrm{TM}} = \frac{r_n^{\mathrm{TM}} + R_{n+1}^{\mathrm{TM}}\exp(-2\Gamma_{n+1}h_{n+1})}{1 + r_n^{\mathrm{TM}}R_{n+1}^{\mathrm{TM}}\exp(-2\Gamma_{n+1}h_{n+1})} \tag{10}$$

$$R_n^{\mathrm{TE}} = \frac{r_n^{\mathrm{TE}} + R_{n+1}^{\mathrm{TE}}\exp(-2\Gamma_{n+1}h_{n+1})}{1 + r_n^{\mathrm{TE}}R_{n+1}^{\mathrm{TE}}\exp(-2\Gamma_{n+1}h_{n+1})} \tag{11}$$

where r_n^{TM} and r_n^{TE} denote the local plane wave TM and TE reflection coefficients at interface n. These local reflection coefficients are defined as follows:

$$r_n^{\mathrm{TM}} = \frac{\eta_{n+1}\Gamma_n - \eta_n\Gamma_{n+1}}{\eta_{n+1}\Gamma_n + \eta_n\Gamma_{n+1}} \tag{12}$$

$$r_n^{\mathrm{TE}} = \frac{\mu_{n+1}\Gamma_n - \mu_n\Gamma_{n+1}}{\mu_{n+1}\Gamma_n + \mu_n\Gamma_{n+1}}. \tag{13}$$

In the spectral domain, the global reflection coefficients of the multilayered medium are derived using a recursive scheme implying the computation of the local reflection coefficients of each interface [35], [36]. The recursive scheme is initiated by assuming that there are no upgoing waves coming from the lower half-space, i.e., that the global reflection coefficient is equal to the local reflection coefficient of the lower half-space interface. The transformation back to the spatial domain is performed using a fast procedure evaluating numerically the semi-infinite integral [37].

III. Antenna Effect Removal Strategy

Under far-field conditions, the homogeneous backscattered field assumption permits to consider that a single dielectric dipole ($M = 1$) holds for describing antenna reflections and transmissions. In this specific case, (7) can be analytically

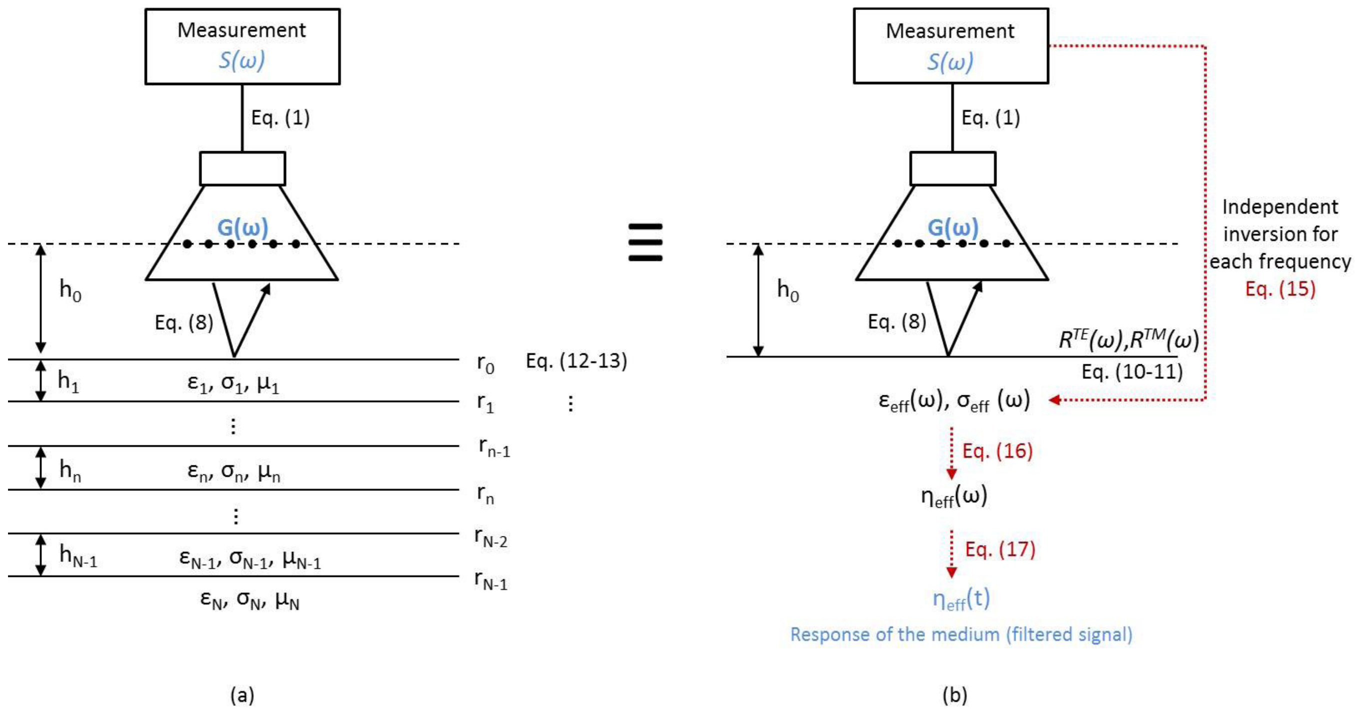

Fig. 1. Strategy used to remove antenna effects from near-field GPR data. (a) Radar above a multilayered medium. (b) Radar above an equivalent half-space medium with frequency-dependent global reflection coefficients.

inverted and Green's functions (filtered signals) can be computed from the radar measurements as follows:

$$G_{11}(\omega) = \frac{S(\omega) - R_i(\omega)}{S(\omega)R_{s,1}(\omega) - R_i(\omega)R_{s,1}(\omega) + T_1(\omega)}. \quad (14)$$

Under near-field conditions, an analytical solution does not exist. Only the free-space antenna response $T_0(\omega)$ can be subtracted from the radar signal. In order to retrieve the medium response free from the antenna effects, a numerical approach has been developed. It is worth noting that this approach is theoretically exact for wave propagation in the multilayered media. When objects are present in the medium, some antenna effects are still present, such as the antenna radiation pattern leading to the typical reflection hyperbolas.

As shown in Fig. 1(a), the magnetic permeability, the dielectric permittivity, and the electrical conductivity are the electromagnetic properties that characterize the layers of a multilayered medium. Knowledge of these medium properties permits to compute the local reflection coefficient at each interface using the recursive procedure detailed through (12) and (13). Applying this recursive scheme up to the upper half-space layer leads to the global reflection coefficients characterizing the multilayered medium. These global reflection coefficients account for all infinite reflections and transmissions occurring within the multilayered medium. The retrieval of the electromagnetic properties of the layers becomes rapidly complex or impossible when increasing the number of layers. However, retrieving an equivalent half-space effective complex conductivity, as depicted in Fig. 1(b), reduces the inverse problem to two unknowns per frequency, independently. This is the proposed strategy to filter out antenna effects.

The inversion problem for each frequency is formulated in the least-squares sense and the objective function to be minimized is accordingly formulated in the frequency domain as follows:

$$\phi_i(\mathbf{b}) = |\mathbf{S}^* - \mathbf{S}|^T |\mathbf{S}^* - \mathbf{S}| \quad (15)$$

where $\phi_i(\mathbf{b})$ is the objective function to be minimized, i is the frequency index, $\mathbf{S}^* = S(\omega_i)$ and $\mathbf{S} = S(\omega_i, \mathbf{b})$ are the vectors containing, respectively, the observed and the simulated radar data, T denotes the transpose, and $\mathbf{b}$ is the parameter vector $[\varepsilon_{\text{eff},i}, \sigma_{\text{eff},i}]$ to be estimated. The antenna height is assumed to be known. The minimization of the objective function involves a sequential combination of the global multilevel coordinate search (GMCS) [38] algorithm with the Nelder–Mead Simplex (NMS) algorithm [39]. GMCS is a global optimization algorithm able to deal with complex topographies and the multimodality of multidimensional nonlinear objective functions without requiring excessive computing resources. NMS is a nonlinear and fast local search algorithm. The combination of these two algorithms represents a robust and efficient optimization approach for minimizing the objective function [40].

Once all inversions have been performed for each frequency, $\varepsilon_{\text{eff}}(\omega)$ and $\sigma_{\text{eff}}(\omega)$ are known and the complex effective conductivities $[\eta_{\text{eff}}(\omega)]$, as found in the frequency-domain Maxwell's equations, can be calculated as

$$\eta_{\text{eff}}(\omega) = \sigma_{\text{eff}}(\omega) + j\omega\varepsilon_{\text{eff}}(\omega). \quad (16)$$

This effective conductivity characterizing the equivalent half-space medium directly determines the global reflection coefficients and, hence, includes all the reflections occurring

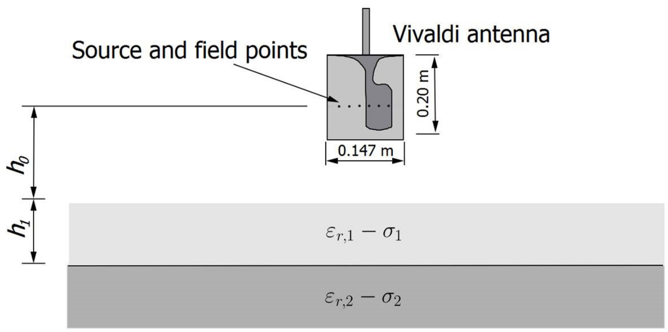

Fig. 2. Configuration used in the numerical experiments: Vivaldi antenna located above a 3-D bilayered medium.

within the multilayered medium. Converting that quantity into the time domain, therefore, provides a signal free from the antenna effects that show these reflections. This operation is performed using the inverse Fourier transform (IFT)

$$\eta_{\text{eff}}(t) = \frac{1}{2\pi} \int_{-\infty}^{\infty} \eta_{\text{eff}}(\omega) e^{j\omega t} d\omega. \tag{17}$$

Therefore, stacking the time-domain complex effective conductivities $\eta_{\text{eff}}(t)$ computed for each position along a radar profile provides the filtered radar image. The proposed procedure is theoretically exact for wave propagation in the layered media. When an object is present, artifacts will arise, but they are expected to remain minor compared to the improvement of the image [5]. Additional extensive analyses involving many different scenarios have to be performed in order to validate this hypothesis and determine its limitations. Depending on the application, the surface reflection can be further removed from the filtered radar data to highlight underlying targets [5]. This step can be done as follows in the frequency domain:

$$\eta_{\text{filt}}(\omega) = \eta_{\text{eff}}(\omega) - \eta_s \tag{18}$$

where $\eta_{\text{filt}}(\omega)$ is the resulting filtered complex conductivity in the frequency domain (from which the surface reflection has been removed) and η_s is the complex conductivity of the top layer ($\eta_s = \sigma_1 + j\omega\varepsilon_1$). The surface reflection removal step requires knowledge of η_s. This term can be computed by focusing the FWI on the surface reflection (see [5], [41]).

IV. Numerical Experiments

A. Model Configuration

Numerical simulations were conducted in order to theoretically demonstrate the concept of the proposed filtering method under the far- and near-field conditions. We used the electromagnetic model presented in Section II-A to simulate the radar waveforms. In (1), the model requires knowledge of the antenna characteristic functions. For this purpose, we used the transfer functions determined for the tapered slot Vivaldi antenna developed by Guillanton *et al.* [42] and Fauchard and Laguerre [43] as example. The antenna, which has an aperture of 0.147 m and a height of 0.2 m, was calibrated by performing 100 measurements at a distance ranging from 0.0 to 0.4 m over a 3 m × 3 m copper plane acting as a perfect electrical conductor (PEC). The antenna was modeled using an equivalent set of six source and field points evenly distributed along a line. As shown in [34], this number of points is expected to be a good tradeoff between modeling accuracy and computation time.

The antenna–medium configuration considered for the simulation scenarios is presented in Fig. 2. The Vivaldi antenna is located above a medium composed of two layers. The upper layer has a thickness h_1 of 30 cm and a relative permittivity $\varepsilon_{r,1}$ equal to 6, whereas the relative permittivity of the lower half-space layer $\varepsilon_{r,2}$ was set to 12. The electrical conductivities of the two layers were both set to 0 S/m. In a first scenario, we simulated a signal acquired at 30 cm over the layered medium. As the far-field conditions are respected, the far-field equation (7) can be used [30]. For the second scenario, the radar waveforms were simulated under the near-field conditions by considering the antenna located at 1, 5, and 10 cm, respectively, above the layered medium. All simulations were performed using 101 frequencies evenly distributed in the frequency range 800–1600 MHz, thereby resulting in a frequency step of 8 MHz.

Inversions were then conducted on the simulated radar waveforms in order to retrieve the complex effective conductivity $\eta_{\text{eff}}(\omega)$. The parameter spaces considered in the inversions were defined as follows: $\varepsilon_{\text{eff}} = [1 \ldots 20]$ and $\sigma_{\text{eff}} = [10^{-4} \ldots 1]$. They were chosen large enough to ensure they contain the solutions. About 300 objective function evaluations were required to solve the inverse problem for each frequency.

B. Numerical Results

1) Far-Field Scenario: The radar signals simulated and filtered using the numerical filtering approach are presented in Fig. 3. The results are compared to the analytical filter (14). The filtered signals were normalized as the represented quantities are physically different (Green's function for the analytical filter and complex effective conductivity for the numerical approach). In particular, a time shift was applied to the Green's function to move time zero, corresponding to the antenna phase center, to the medium surface, corresponding to time zero of $\eta(t)$. The results show that the surface reflection is the same for both the methods. The second reflection corresponding to the interface between the two layers is located at about 5 ns. The propagation times are the same for both the methods and in agreement with the expected value assuming straight ray propagation. Regarding amplitudes, minor differences between the two methods are observed. These differences are mainly detected around 10 ns, which corresponds to the first multiple reflection. These differences are attributed to the fact that both waveforms represent different physical quantities.

Fig. 4 shows, for the numerical method, the absolute difference between the measured and the modeled signals in the frequency domain. The error periodically oscillates between $10^{-2.19}$ and $10^{-10.31}$. These error values are in general relatively small in terms of radar dynamic range. The objective function (15) pertaining to the cases with low and high error values is presented in Fig. 5. To better highlight their topographies, the objective function values are expressed in a logarithmic scale. The objective function topography

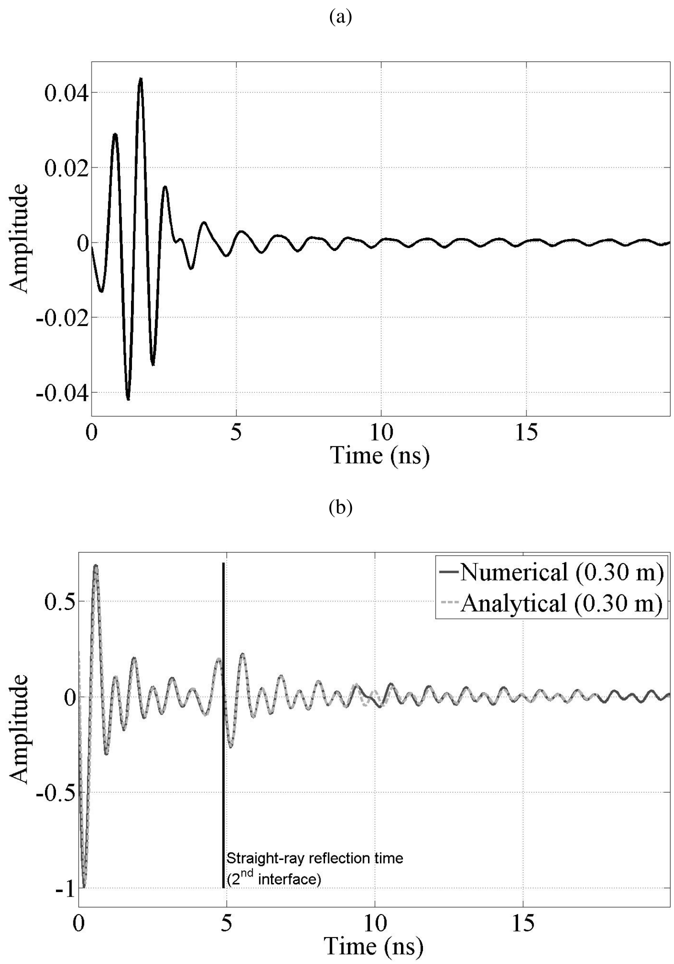

Fig. 3. Comparison between (a) simulated radar data and (b) signals processed with the far-field analytical and numerical antenna effects removal approaches.

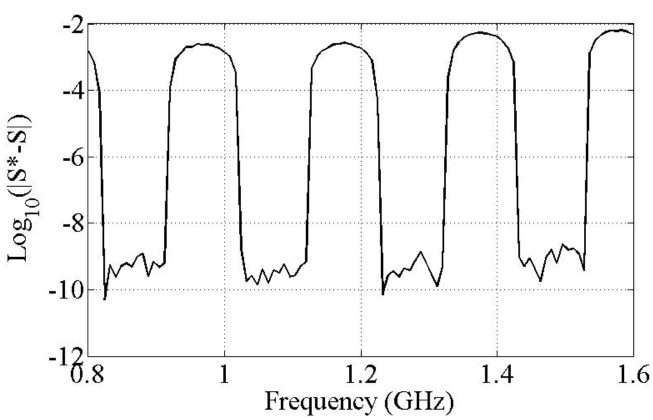

Fig. 4. Absolute value of the difference between the measured and modeled signals as a function of frequency for the first scenario.

related to the 1.44-GHz frequency shows a well-defined global minimum. In contrast, the objective function regarding the 1.60-GHz frequency evidences a poor sensitivity to the effective conductivity σ_{eff} below about $10^{-1.5}$ S/m, which results in larger numerical errors during the optimization.

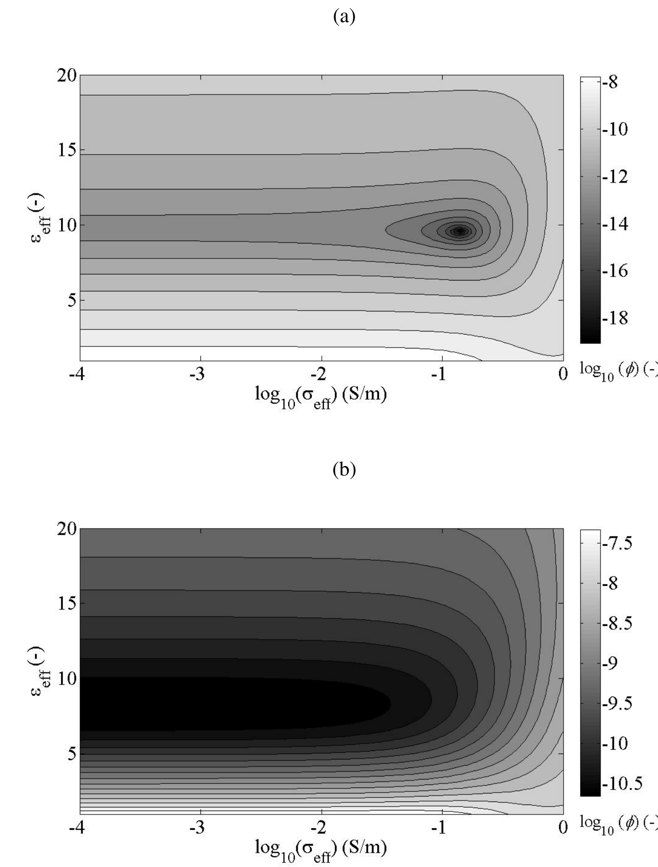

Fig. 5. Objective functions for (a) 1.4-GHz (relatively small misfit) and (b) 1.6-GHz (relatively large misfit) frequencies.

2) Near-Field Scenario: The radar measurements simulated for the near-field conditions are shown in Fig. 6(a). The far-field case is also presented for comparison. As can be seen, the antenna effects prevent to detect or precisely locate the reflection interfaces. Once filtered using the proposed method [Fig. 6(b)], the reflections clearly appear and the propagation times specific to the different interfaces can be determined. In theory, regardless of the antenna height, the filtered signals should be identical for the same medium. However, we observe some differences. In particular, the amplitude of the second interface reflection slightly decreases with the increasing antenna height. This is to be attributed to numerical errors in the inverse problem due to the lack of sensitivity for specific frequencies. Despite these minor limitations, these results demonstrate the proposed concept under both the far- and near-field conditions. They evidence that the filtered radar data represent much better the medium structures compared to the measured signals which include antenna internal reflections and antenna–medium coupling. The resolution is also improved.

V. Laboratory Experiments

A. Setup and Acquisition Procedure

Laboratory experiments were conducted in the Hydrogeophysics Laboratory of the Université catholique

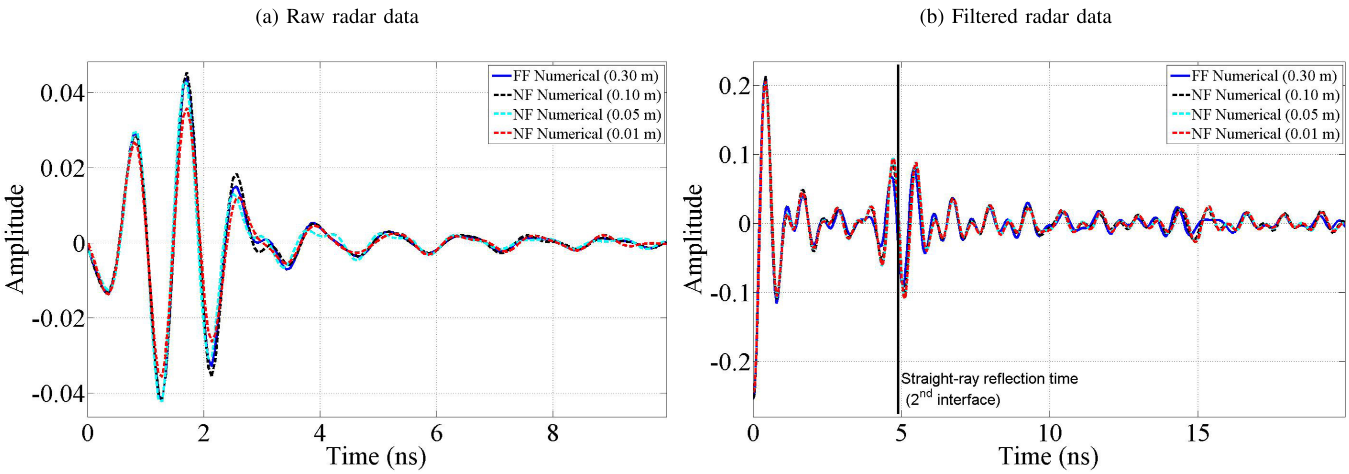

Fig. 6. Comparison between (a) simulated radar data and (b) corresponding filtered signals under near- and far-field conditions.

de Louvain (http://sites.uclouvain.be/gprlouvain) in order to test the proposed method on real radar data sets. We used a stepped-frequency continuous-wave radar system composed of a tapered slot Vivaldi antenna [42], [43] (the same as used for the numerical experiments) and a vector network analyzer (VNA, ZNB8, Rhode & Schwarz, Munich, Germany). The antenna was calibrated as described in Lambot and André [32].

It is worth noting that the radar equations similarly apply as well to time-domain radars [44]. The antenna acted as a transmitter–receiver unit and was connected by a 50-Ω impedance coaxial cable to the reflection port of the VNA. The VNA was calibrated at the connection between the antenna feed point and the coaxial cable using a standard Open-Short-Match calibration kit. We performed measurements in the frequency range 600–4000 MHz with a frequency step of 20 MHz for the far-field measurements and 40 MHz for the near-field measurements, thereby resulting in 171 and 86 frequencies, respectively. We used fewer frequencies in the near-field experiments to limit computation time as we used only one processor in this paper. We refer to De Coster *et al.* [40] regarding the optimization of the number of frequencies required to solve a particular inverse problem.

The measurements were performed over a 3 m × 3 m × 1 m sandbox in which three plastic pipes filled with air were buried (Fig. 7). The pipes were 1.2 m long and had an outer diameter of 0.05 m. They were located at 0.069, 0.287, and 0.506 m from the sand surface. A copper sheet acting as a PEC was placed below the sandbox to avoid unidentified reflections coming from the underlying materials. Two profiles of 2.41 m long each were acquired with the antenna at 0.05 m (near field) and 0.2 m (far field) above the sand, respectively. The sampling density was set to 100 scans per meter. The radar system was fixed on a xyz-automated positioning table. We used a computer to automatically control the acquisition process.

The antenna height above the sand surface as well as the sand surface permittivity were determined independently for each position using FWIs focused on the surface reflection. The electrical conductivity of the dry sand was set to 0 S/m.

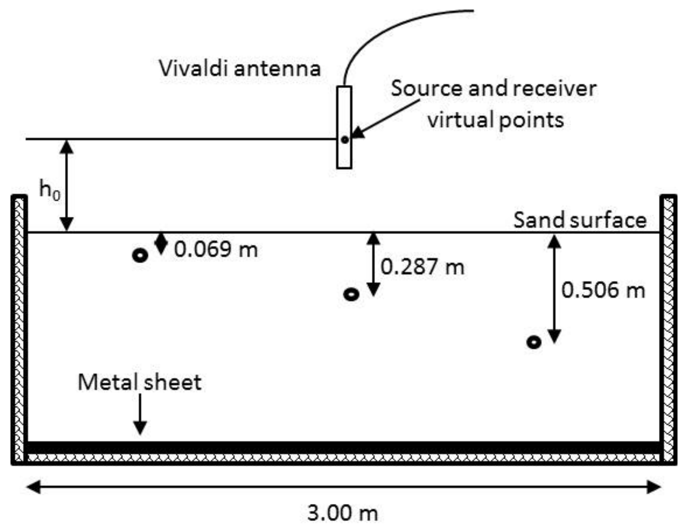

Fig. 7. Laboratory setup: Vivaldi antenna above a 3 m × 3 m × 1 m sandbox in which three empty plastic pipes were buried.

The permittivity and conductivity of the sand surface were used to calculate η_s in (18). This quantity was then used to filter out the surface reflection. The proposed method was compared with the common BS approach using the mean trace subtraction (MTS). The MTS approach consists in calculating the average signal across the entire profile and to subtract it from each measurement. From a physical point of view, this removes T_0 from radar data [see (1)] but also removes constant reflectors and introduces distortions in the radar images.

B. Laboratory Results

1) Far Field: Fig. 8(a) shows the radar measurements acquired over the sandbox with the antenna aperture at 20 cm above the sand surface. The constant reflection from the PEC is visible at around 12.15 ns. The reflection hyperbolas originating from the pipes are much less visible and are partly overwhelmed by the antenna internal reflections. Fig. 8(c)

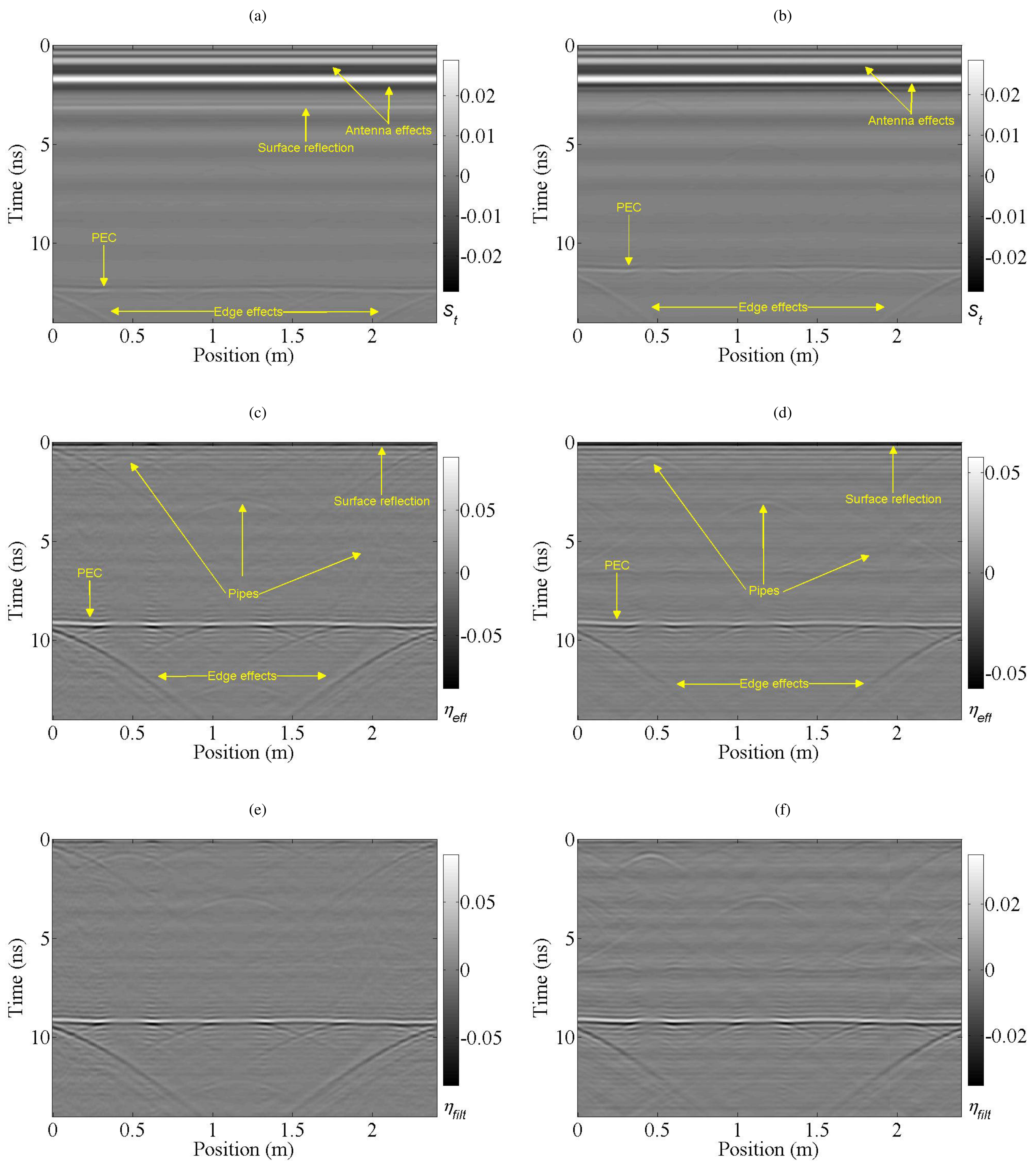

Fig. 8. Image of (a) and (b) radar measurements, (c) and (d) complex effective conductivity $\eta_{\text{eff}}(t)$ and complex conductivity without the surface reflection $\eta_{\text{filt}}(t)$ for measurements performed at about 20 cm (far-field) and 5 cm (near-field) above de sandbox. (a) Radar data in the time domain $S(t)$ ($h_0 = 20$ cm). (b) Radar data in the time domain $S(t)$ ($h_0 = 5$ cm). (c) $\eta_{\text{eff}}(t)$ ($h_0 = 20$ cm). (d) $\eta_{\text{eff}}(t)$ ($h_0 = 5$ cm). (e) $\eta_{\text{filt}}(t)$ ($h_0 = 20$ cm). (f) $\eta_{\text{filt}}(t)$ ($h_0 = 5$ cm).

shows the corresponding radar image after having filtered out antenna reflections [$\eta_{\text{eff}}(t)$]. We observe that: 1) the surface reflection is constant and clearly identified at time zero despite the slightly changing antenna height; 2) the antenna internal reflections are removed; and 3) the antenna–medium multiple reflections are also removed. As a result, the reflections of the PEC and pipes are more clearly visible compared with the original image. A slight aliasing effect is nonetheless seen in the filtered image. It results from the IFT and the limited frequency range.

Fig. 8(e) shows the radar image after having further removed the surface reflection (18). The results indicate that $\varepsilon_{r,1}$ was

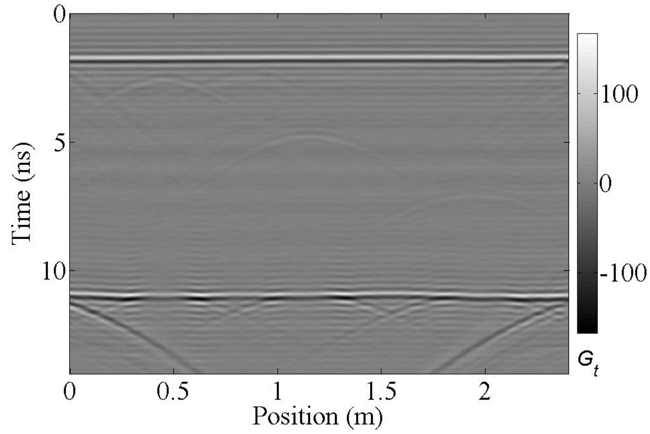

Fig. 9. Image of the analytically filtered data (Green's functions—G) for measurements performed at about 20 cm (far-field) above the sand surface.

accurately retrieved because the surface reflection completely vanished. The relative permittivity retrieved by inversion oscillates between 2.35 and 2.82 as a result of the inherent variability of the sand density in the sandbox. These relatively low permittivities, characteristic of a dry sand, explain why the reflections originating from the pipes filled with air ($\varepsilon = 1$) are not stronger. Fig. 8(e) shows that removing the surface reflection slightly improves the contrast of the reflection hyperbolas. It is worth noting that the filtering procedure does not remove antenna radiation pattern effects which lead to the hyperbolas.

Fig. 9 shows the radar image analytically obtained through (14). It is worth noting that time zero corresponds now to the antenna phase center. Compared to Fig. 8(c), the results are similar. The oblique reflections from the edges of the sandbox are more visible in the $\eta(t)$ image. We computed the two-way travel time between the sand surface and the three pipes after applying the analytical and numerical filtering methods. The results show a difference of about 0.02 ns, which corresponds to 0.2 cm considering an average relative permittivity of 2.75. The computation time required to evaluate (14) on the whole profile is of the order of the second (real-time processing) while it reaches about one day for the numerical approach (Intel Core CPU 3.60 GHz, MATLAB environment). Practical applications of the proposed method therefore require parallel computing, which is straightforward to implement as each frequency represents an independent inverse problem.

The image resulting from the classical average background removal is shown in Fig. 10(a). We observe that the amplitude of the hyperbolas originating from the pipes are, in this case, more contrasted than those obtained with the physical antenna effect removal approach. This is, for this particular example, more advantageous in terms of detection, but it can be misleading regarding the actual dielectric contrast between the pipes and the surrounding material. In addition, the surface reflection is not entirely removed due to the slight slope observed for the sand surface. The presence of surface roughness would make the surface reflection removal worse. Finally, it distorts the reflection from the PEC at the bottom of the sandbox. The possibility of determining the depth of the objects from the straight ray propagation times is an additional advantage of the proposed filtering technique compared to the average BS method. Indeed, propagation times are referenced (e.g., time zero) and remain physically consistent.

2) Near Field: The raw radar data acquired over the sandbox with the antenna aperture placed at 5 cm above the sand surface are shown in Fig. 8(b). Under near-field conditions, the reflection of the shallowest pipe is partly mixed with the surface reflection and antenna reflection, thereby making more difficult the detection of the pipe. For the rest, the image is similar to the one obtained under far-field conditions. Only propagation times are different.

The results obtained with the proposed antenna filtering method are shown in Fig. 8(d). The surface reflection is well defined and the antenna internal reflections and antenna–medium multiple reflections are efficiently removed. The reflection hyperbolas are also better contrasted compared with the original radar measurements, except for the deepest pipe for which the hyperbola does not clearly appear as such. This is attributed to the relatively low signal-to-noise ratio for that reflection which has led to more significant numerical errors in the inverse filtering procedure. As expected, the edge effects are nonetheless less marked here than under far-field conditions.

As a benchmark, we simulated an ideal filtered radar image of the scene, i.e., an image of what the radar data should look like if we would not consider antenna effects. This synthetic image was generated by implementing the laboratory setup characteristics in the gprMax software [45] and removing the global transmission/reflection coefficient of the antenna in free space (T_0) from the simulated data. The resulting image (Fig. 11) is quite similar to Fig. 8(d) even if some noise inherent to real measurements are observed in the numerically filtered image. The apex of the hyperbolas is located at the same depths. The amplitude contrasts of the reflection hyperbolas are in general respected although the deepest pipe reflection showed in Fig. 8(d) is less pronounced than in the ideal case. The shape of the hyperbolas is also comparable even though the branches of the two deepest ones are shorter in Fig. 8(d). The comparison between the ideal and measured filtered images demonstrated the efficiency of the antenna effects removal proof of concept even if some adjustments are still needed to provide ideal images under near-field conditions.

The further removal of the dominant surface reflection using (18) is shown in Fig. 8(f). This step clearly enhances the amplitude of the reflections originating from the pipes and the PEC. Even if the shallowest pipe was relatively close to the soil surface, the shape and the amplitude of its reflection are well visible. Finally, we observe that the depths of the pipes are identical to those retrieved under far-field conditions, which highlights the robustness of the proposed method under the more complex near-field conditions.

Fig. 10(b) shows the results obtained from the mean average subtraction method. As for the far-field conditions, the reflection hyperbolas are more contrasted. The surface reflection is not well removed and the remaining amplitudes do not properly represent the air–sand dielectric contrasts. Similar observations can be made for the PEC reflections, which do

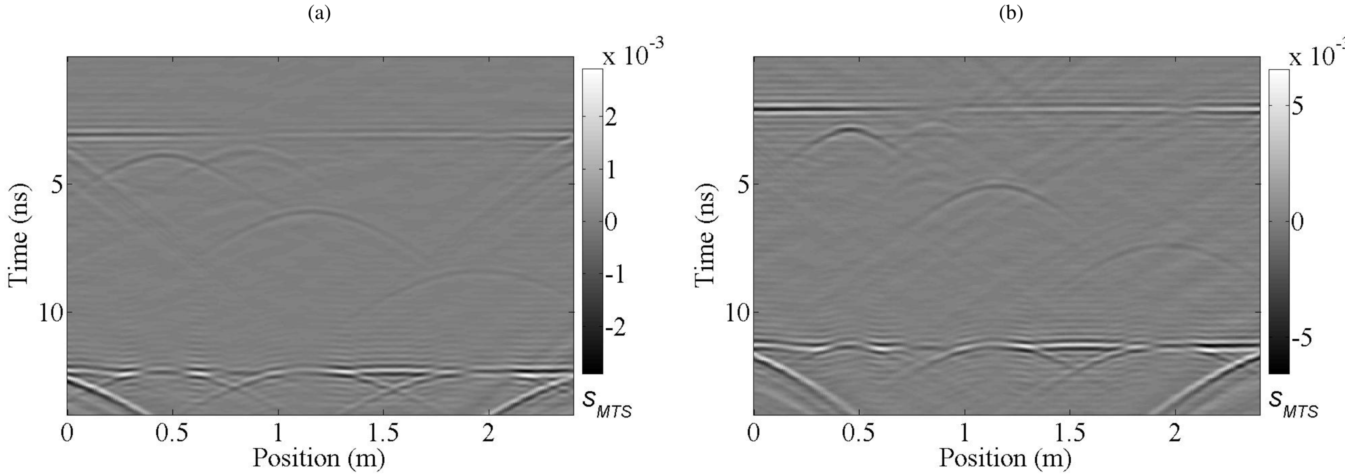

Fig. 10. Image resulting from the MTS for measurements performed at about (a) 20 cm (far-field) and (b) 5 cm (near-field) above the sand surface.

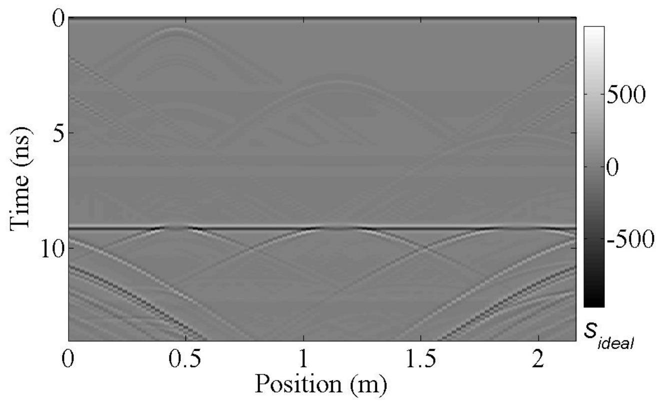

Fig. 11. Ideal filtered image considering measurements performed at 5 cm above the sand surface (near-field).

not represent correctly the sand-PEC dielectric contrasts along the profile.

VI. Conclusion

We proposed a novel physically based approach for filtering out the antenna multiple internal reflections and antenna–medium ringing from the GPR data acquired under near-field conditions. The proposed methodology relies on the intrinsic radar equation of Lambot and André [32] and on a full-wave inverse modeling procedure. The radar model in particular includes antenna internal reflections and antenna–medium coupling. The proposed approach relies on the mathematical fact that any multilayered medium can be reduced to a half-space medium characterized by frequency-dependent global reflection coefficients. The radar data are inverted independently for each frequency to retrieve the complex, effective conductivity of an equivalent half-space medium. Once converted into the time domain, that quantity represents the filtered radar image.

In addition to the removal of the antenna internal and antenna–medium reflections, the proposed filtering approach presents several benefits of interest compared with the traditional average background removal approach: 1) it is a physically based approach that is theoretically exact for locally planar layered media; 2) it does not remove neither alter the constant reflectors (layers, longitudinal pipes, etc.); 3) it allows determining the depths of the objects with a better accuracy; 4) it moves the usually ambiguous time zero to the first medium interface; and 5) it allows removing the surface reflection independently for each signal, which facilitates the detection of small objects buried close to the surface (landmines). Future research will focus on the numerical optimization scheme improvement and on the application of the method to time-domain radars.

References

[1] E. Slob, M. Sato, and G. Olhoeft, "Surface and borehole ground-penetrating-radar developments," *Geophysics*, vol. 75, no. 5, pp. 75A103–75A120, Sep. 2010.

[2] A. P. Annan, "GPR—History, trends, and future developments," *Subsurface Sens. Technol. Appl.*, vol. 3, no. 4, pp. 253–270, Oct. 2002.

[3] D. Daniels, *Ground Penetrating Radar* (IEE Radar, Sonar, Navigation and Avionics Series), 2nd ed. London, U.K.: IET, 2004, p. 726.

[4] H. M. Jol, *Ground Penetrating Radar Theory and Applications*. Amsterdam, The Netherlands: Elsevier, 2009, p. 544.

[5] O. Lopera, E. C. Slob, N. Milisavljević, and S. Lambot, "Filtering soil surface and antenna effects from GPR data to enhance landmine detection," *IEEE Trans. Geosci. Remote Sens.*, vol. 45, no. 3, pp. 707–717, Mar. 2007.

[6] F. Soldovieri, O. Lopera, and S. Lambot, "Combination of advanced inversion techniques for an accurate target localization via GPR for demining applications," *IEEE Trans. Geosci. Remote Sens.*, vol. 49, no. 1, pp. 451–461, Jan. 2011.

[7] P. A. van Vuuren, "Landmine detection by means of ground penetrating radar: A model-based approach," *Afr. Res. J.*, vol. 105, no. 3, pp. 4–17, Sep. 2014.

[8] G. F. Stickley, D. A. Noon, M. Cherniakov, and I. Longstaff, "Gated stepped-frequency ground penetrating radar," *J. Appl. Geophys.*, vol. 43, nos. 2–4, pp. 259–269, Mar. 2000.

[9] H. Brunzell, "Detection of shallowly buried objects using impulse radar," *IEEE Trans. Geosci. Remote Sens.*, vol. 37, no. 2, pp. 875–886, Mar. 1999.

[10] J. Groenenboom and A. Yarovoy, "Data processing and imaging in GPR system dedicated for landmine detection," *Subsurface Sens. Technol. Appl.*, vol. 3, no. 4, pp. 387–402, Oct. 2002.

[11] M. Piccardi, "Background subtraction techniques: A review," in *Proc. IEEE Int. Conf. Syst., Man Cybern.*, The Hague, The Netherlands, vol. 4, Oct. 2004, pp. 3099–3104.

[12] F. Roth, P. van Genderen, and M. Verhaegen, "Processing and analysis of polarimetric ground penetrating radar landmine signatures," in *Proc. 2nd Int. Workshop Adv. Ground Penetrating Radar*, Delft, The Netherlands, May 2003, pp. 70–75.

[13] A. M. Mayordomo and A. Yarovoy, "Optimal background subtraction in GPR for humanitarian demining," in *Proc. 5th Eur. Radar Conf.*, Amsterdam, The Netherlands, Oct. 2008, pp. 48–51.

[14] J. W. Brooks, L. M. van Kempen, and H. Sahli, "A primary study in adaptative clutter reduction and buried minelike target enhancement from GPR data," *Proc. SPIE*, vol. 4038, pp. 1183–1192, Aug. 2000.
[15] M. El-Shenawee and C. M. Rappaport, "Monte Carlo simulations for clutter statistics in minefields: AP-mine-like-target buried near a dielectric object beneath 2-D random rough ground surfaces," *IEEE Trans. Geosci. Remote Sens.*, vol. 40, no. 6, pp. 1416–1426, Jun. 2002.
[16] A. V. D. Merwe and I. J. Gupta, "A novel signal processing technique for clutter reduction in GPR measurements of small, shallow land mines," *IEEE Trans. Geosci. Remote Sens.*, vol. 38, no. 6, pp. 2627–2637, Nov. 2000.
[17] F. Abujarad and A. Omar, "GPR data processing using the component-separation methods PCA and ICA," in *Proc. IEEE Int. Workshop Imag. Syst. Techn.*, Minori, Italy, Apr. 2006, pp. 60–64.
[18] B. Karlsen, J. Larsen, H. B. D. Sorensen, and K. B. Jakobsen, "Comparison of PCA and ICA based clutter reduction in GPR systems for anti-personal landmine detection," in *Proc. 11th IEEE Signal Process. Workshop Stat. Signal Process.*, Aug. 2001, pp. 146–149.
[19] E. Tebchrany, F. Sagnard, V. Baltazart, J.-P. Tarel, and X. Dérobert, "Assessment of statistical-based clutter reduction techniques on ground-coupled GPR data for the detection of buried objects in soils," in *Proc. 15th Int. Conf. Ground Penetrating Radar*, Brussels, Belgium, Jun./Jul. 2014, pp. 604–609.
[20] S. Tjora, E. Eide, and L. Lundheim, "Evaluation of methods for ground bounce removal in GPR utility mapping," in *Proc. 10th Int. Conf. Ground Penetrating Radar*, Delft, The Netherlands, Jun. 2004, pp. 379–382.
[21] A. Zhao, Y. Jiang, W. Wang, and X. Jiaotong, "Exploring independent component analysis for GPR signal processing," in *Proc. Prog. Electromagn. Res. Symp.*, Hangzhou, China, Aug. 2005, pp. 750–753.
[22] D. Potin, E. Duflos, and P. Vanheeghe, "Landmines ground-penetrating radar signal enhancement by digital filtering," *IEEE Trans. Geosci. Remote Sens.*, vol. 44, no. 9, pp. 2393–2406, Sep. 2006.
[23] D. Carevic, "Kalman filter-based approach to target detection and target-background separtion in ground-penetrating radar data," *Proc. SPIE*, vol. 3710, pp. 1284–1288, Aug. 1999.
[24] Y. Luo and G.-Y. Fang, "GPR clutter reduction and buried target detection by improved Kalman filter technique," in *Proc. Int. Conf. Mach. Learn. Cybern.*, Guangzhou, China, vol. 9, Aug. 2005, pp. 5432–5436.
[25] L. M. van Kempen and H. Sahli, "Signal processing techniques for clutter parameters estimation and clutter removal in GPR data for landmine detection," in *Proc. 11th IEEE Signal Process. Workshop Stat. Signal Process.*, Aug. 2001, pp. 158–161.
[26] A. M. Zoubir, I. J. Chant, C. L. Brown, B. Barkat, and C. Abeynayake, "Signal processing techniques for landmine detection using impulse ground penetrating radar," *IEEE Sensors J.*, vol. 2, no. 1, pp. 41–51, Feb. 2002.
[27] L. Gurel and U. Oguz, "Optimization of the transmitter-receiver separation in the ground-penetrating radar," *IEEE Trans. Antennas Propag.*, vol. 51, no. 3, pp. 362–370, Mar. 2003.
[28] R. Persico and F. Soldovieri, "A microwave tomography approach for a differential configuration in GPR prospecting," *IEEE Trans. Antennas Propag.*, vol. 54, no. 11, pp. 3541–3548, Nov. 2006.
[29] R. Persico, G. Pochanin, V. Ruban, A. Orlenko, I. Catapano, and F. Soldovieri, "Performances of a microwave tomographic algorithm for GPR systems working in differential configuration," *IEEE J. Sel. Topics Appl. Earth Observ. Remote Sens.*, vol. 9, no. 4, pp. 1343–1356, Apr. 2016.
[30] S. Lambot, E. C. Slob, I. V. D. Bosch, B. Stockbroeckx, and M. Vanclooster, "Modeling of ground-penetrating Radar for accurate characterization of subsurface electric properties," *IEEE Trans. Geosci. Remote Sens.*, vol. 42, no. 11, pp. 2555–2568, Nov. 2004.
[31] A. P. Tran, F. André, C. Craeye, and S. Lambot, "Near-field or far-field full-wave ground penetrating radar modeling as a function of the antenna height above a planar layered medium," *Prog. Electromagn. Res.*, vol. 141, pp. 415–430, Jul. 2013.
[32] S. Lambot and F. André, "Full-wave modeling of near-field radar data for planar layered media reconstruction," *IEEE Trans. Geosci. Remote Sens.*, vol. 52, no. 5, pp. 2295–2303, May 2014.
[33] S. Lambot, "Method and device for characterization of physical properties of a target volume by electromagnetic inspection," U.S. Patent 2014 0019050 A1, Jan. 16, 2014.
[34] A. P. Tran, F. André, and S. Lambot, "Validation of near-field ground-penetrating radar modeling using full-wave inversion for soil moisture estimation," *IEEE Trans. Geosci. Remote Sens.*, vol. 52, no. 9, pp. 5483–5497, Sep. 2014.
[35] E. Slob and J. Fokkema, "Coupling effects of two electric dipoles on an interface," *Radio Sci.*, vol. 37, no. 5, pp. 1–10, Oct. 2002.
[36] K. A. Michalski and J. R. Mosig, "Multilayered media Green's functions in integral equation formulation," *IEEE Trans. Antennas Propag.*, vol. 45, no. 3, pp. 508–519, Mar. 1997.
[37] S. Lambot, E. Slob, and H. Vereecken, "Fast evaluation of zero-offset Green's function for layered media with application to ground-penetrating radar," *Geophys. Res. Lett.*, vol. 34, no. 21, p. L21801, Nov. 2007.
[38] W. Huyer and A. Neumaier, "Global optimization by multilevel coordinate search," *J. Global Optim.*, vol. 14, no. 4, pp. 331–355, Jun. 1999.
[39] J. C. Lagarias, J. A. Reeds, M. H. Wright, and P. E. Wright, "Convergence properties of the Nelder–Mead simplex method in low dimensions," *SIAM J. Optim.*, vol. 9, no. 1, pp. 112–147, 1998.
[40] A. De Coster, A. P. Tran, and S. Lambot, "Fundamental analyses on layered media reconstruction using GPR and full-wave inversion in near-field conditions," *IEEE Trans. Geosci. Remote Sens.*, vol. 54, no. 9, pp. 5143–5158, Sep. 2016.
[41] S. Lambot, L. Weihermüller, J. A. Huisman, H. Vereecken, M. Vanclooster, and E. Slob, "Analysis of air-launched ground-penetrating radar techniques to measure the soil surface water content," *Water Resour. Res.*, vol. 42, no. 11, p. W11403, Nov. 2006.
[42] E. Guillanton, J. Y. Dauvignac, C. Pichot, and J. Cashman, "A new design tapered slot antenna for ultra-wideband applications," *Microw. Opt. Technol. Lett.*, vol. 19, no. 4, pp. 286–289, Nov. 1998.
[43] C. Fauchard, B. Beaucamp, and L. Laguerre, "Non-destructive assessment of hot mix asphalt compaction/density with a step-frequency radar: Case study on a newly paved road," *Near Surf. Geophys.*, vol. 13, no. 3, pp. 289–297, Jun. 2015.
[44] M. R. M. Ardekani and S. Lambot, "Full-wave calibration of time- and frequency-domain ground-penetrating radar in far-field conditions," *IEEE Trans. Geosci. Remote Sens.*, vol. 52, no. 1, pp. 664–678, Jan. 2014.
[45] A. Giannopoulos, "Modelling ground penetrating radar by GprMax," *Construction Building Mater.*, vol. 19, no. 10, pp. 755–762, Dec. 2005.

Albéric De Coster received the M.Sc. and Ph.D. degrees in agricultural and environmental engineering from the Université catholique de Louvain, Louvain-la-Neuve, Belgium, in 2012 and 2017, respectively. He is a part of COST Action TU1208 Civil Engineering Applications of Ground Penetrating Radar.

His research interests include subsurface imaging, hydrogeophysics, electromagnetic modeling for ground-penetrating radar (GPR), and inversion for nondestructive characterization of soils and materials.

Dr. De Coster was a part of the Organizing Committee of the 15th International Conference on GPR in 2014. He was a recipient of an Early Stage Researcher Award in the same conference.

Sébastien Lambot (M'13) received the M.Sc. *(magna cum laude)* and Ph.D. *(summa cum laude)* degrees in agricultural and environmental engineering from the Université catholique de Louvain (UCL), Louvain-la-Neuve, Belgium, in 1999 and 2003, respectively.

From 2004 to 2005, he was a European Marie-Curie Post-Doctoral Scientist with the Delft University of Technology, Delft, The Netherlands. From 2006 to 2012, he was a Research Group Leader with Forschungszentrum Jlich, Jlich, Germany. Since 2006, he has been a Professor and an FNRS Research Group Leader with UCL. His research interests include electromagnetic modeling for ground-penetrating radar (GPR) and electromagnetic induction, inversion for nondestructive characterization of soils and materials, hydrogeophysics, and remote sensing of the environment. He has authored or co-authored more than 70 journal papers on these topics.

Dr. Lambot was the General Chair of the 3rd International Workshop on Advanced GPR in 2005 and the General Chair of the 15th International Conference on GPR in 2014. He has organized GPR and Hydrogeophysics sessions in the GPR, IWAGPR, AGU, EGU, CMWR, and EAGE international conferences. He was a Guest Editor for four Special Issues in *Near Surface Geophysics*, the *Vadose Zone Journal*, and the IEEE JOURNAL OF SELECTED TOPICS IN APPLIED EARTH OBSERVATIONS AND REMOTE SENSING (JSTARS). He was an Associate Editor of the *Vadose Zone Journal* from 2009 to 2014. He is currently an Associate Editor of the IEEE JSTARS.